Journal of Industrial and Engineering Chemistry
Volume 87, 25 July 2020, Pages 250-263

Novel metal–organic framework of UTSA-16 (Zn) synthesized by a microwave method: Outstanding performance for CO_2 capture with improved stability to acid gases

Sanjit Gaikwad [a], Seok-Jhin Kim [b], Sangil Han [a]

https://doi.org/10.1016/j.jiec.2020.04.015

Abstract

Herein we present a novel metal–organic framework (UTSA-16 (Zn)), where cobalt in the framework is replaced by zinc via microwave irradiation, with significantly improved stability in humid air and acid gases and better selectivity (CO_2/N_2) than the original Co-containing framework. The synthesis was performed using microwave irradiation by changing the irradiation time from 1 to 6 h. The integrities of the frameworks were assessed with scanning electron microscopy for particle morphology, powder X-ray diffraction for crystal integrity, Brunauer–Emmett–Teller for structural properties, and thermogravimetric analysis for thermal stability. An irradiation time of 4 h produced 4h-UTSA-16 with an outstanding CO_2 adsorption capacity of 4.71 mmol/g at 298 K and 1 bar and with CO_2/N_2 selectivity of 118. The improvement in stability and CO_2/N_2 sorption selectivity of UTSA-16 (Zn) over the parent UTSA-16 (Co) was not compromised by decreases in CO_2 uptake after exposure to humid air, SO_2, and NO_2 gases. Further, analysis of production cost showed that the UTSA-16 (Zn) is superior to other adsorbents for CO_2 capture.

Graphical abstract

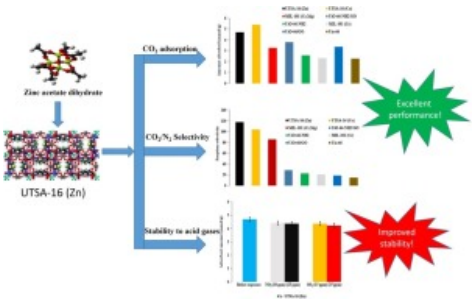

Keywords

Adsorption; Metal–organic frameworks; Microwave; UTSA-16; Acid gases

Introduction

CO_2 is the primary greenhouse gas responsible for global warming, and global CO_2 emissions are predominately caused by fossil fuels during electricity generation. To maintain global temperature increases between 2.48 and 2.88 °C, CO_2 concentration in the atmosphere should be suppressed below 450 ppm [1]. CO_2 capture and storage as a CO_2 control option can substantially contribute to reducing CO_2 levels to target emission of 30–60% of that measured in 2000 by 2050. Global CO_2 emissions have continued to increase gradually throughout the century due to the combustion of carbon-based fuels (coal, natural gas, and oil) as well as chemical reactions in steel, cement, and petrochemical industries [2]. With regard to energy use and environmental conservation, providing energy while reducing CO_2 emissions with efficient technology is one of the most demanding needs of a global society. Among CO_2 emission control strategies such as pre-combustion, post-combustion, and oxy-combustion technologies, post-combustion technology is an attractive method as it is easily applicable to existing fossil fuel-based power plants.

Among chemical separation processes, such as chemical and physical adsorption and membrane separation [3], chemical absorption with amine solutions has been widely used for CO_2 capture in petrochemical processes. However, amine aqueous solutions suffer from disadvantages like metal instruments corrosion, the high energy requirement for the regeneration process, and complicated processes with a large volume. According to reviews on CO_2 [4], [5], a compromising CO_2 capture sorbent for practical applications should provide low production cost, high CO_2 molecular diffusion, high CO_2 sorption capacity, and CO_2/N_2 sorption selectivity as well as stability to impurities in the flue gas.

To overcome challenges in the chemical adsorption process, a large number of porous adsorbents have been designed as high-capacity adsorbents including zeolite, activated carbon, and metal–organic frameworks (MOFs) [6], [7]. The main criteria for adsorbent selections are a large ratio of surface area to weight, high uptake capacity and sorption selectivity, and stability. MOFs, made up of metal ions and organic ligands to form a highly ordered porous framework, are one of the most compromising organic–inorganic porous materials. The unique properties in MOF materials are due to their physical and chemical properties like uniform pore size distribution, tuneable functionality, and large surface area. MOFs possess promising capabilities for many applications including gas adsorption, separation, catalysis [8], [9], medical application [10], [11], optical application [12], and electronic materials [13]. Their potential continues to rise due to the unlimited number of coordination binding of metal and organic linkers as well as the simple modification of MOFs, which in turn, make them promising materials as an adsorbent for CO_2 capture.

Modification of MOFs by doping metal ions have been used for improving the separation performance, and the applicability of this method has been shown by some researchers. Jiao et al. [14] reported that MM-MOF-74, in which different metal ions (Mg^{2+}, Ni^{2+}, and Co^{2+}) had been incorporated, resulting in improvement in CO_2 adsorption. Botas et al. modified MOF-5 with the addition of Co, showing a 17% increase in CO_2 uptake over parent MOF-5 [15]. Bae et al. designed a Li-doped MOF for a 13% increase in CO_2 uptake while a negligible change in CH_4 uptake, thus an improvement in CO_2/CH_4 selectivity [16]. Cao et al. [17] specified that HKUST-1 doped with K^+ showed an 11% rise in CO_2 uptake over the HKUST-1 without K^+ ions. Further, Wei et al. reported that by replacing the metal form of Zn to Cu, the new MOF PCN-922(Cu) showed better performance in gas adsorption and stability compared to the parent PCN-921(Zn) [18].

In another aspect, surface functionalization by changing organic ligands has been proposed as a technique for improving the adsorption and stability properties of MOFs. To improve CO_2 adsorption capacity based on acid–base reaction, NH_2 functional groups are often combined with MOF linkers [19]. The stabilities of certain MOFs were improved by surface functionalization with CH_3 due to preventing water molecules from nearby metal clusters [20]. Deng et al. reported that the functionalization with multiple organics on MOF-5 improved uptake capacities of H_2 and CO_2 compared with the unfunctionalized MOF-5 [21]. Besides, pillar-shaped ligands were used to provide an improved accessibility of amine/amide functional groups in interpenetrated structures of MOFs [22], resulting in an improved adsorption selectivity of CO_2/N_2.

There are several techniques for synthesizing MOFs including solvothermal, sol–gel, microwave (MW), electrochemical, ultrasound, and mechanical methods depending on the energy source to proceed with the formation of the crystalline structure by metal and organic linkers [23], [24], [25]. Masoomi et al. reported mechanosynthesis method for the synthesis of TMU-4,5 with azine-functionalized pores [26], where charged pores in the MOFs provided an effective interaction between host and guest molecules for enhanced adsorption capacities [26], [27]. MW techniques involve ionic conduction and dipole rotation for shifting the energy to solvent being heated without heating a reactor. This results in characteristic properties of MW such as fast crystallization, distribution, efficiency, particle size control, and small particle size [28], [29]. For example, Khan et al. investigated reaction mechanism for the synthesis of Cu-BTC using microwave irradiation and conclude that rapid synthesis is mainly dependent on rapid nucleation rather than rapid crystal growth [30] and Albuquerque et al. synthesized MOF-74 (Ni) by a microwave method using benzoic acid as chemical modular to reduce reaction time for the removal of metal ion from aqueous solution [31]. Chen et al. synthesized MOF-74 (Ni) with a rapid synthesis time of 1 h compared to 32 h for condensation reflux method and 24 h for hydrothermal method [32], while Jhung et al. prepared Cr-MIL-101 and showed that crystallization time can control particle size [33]. Sargazi et al. [34], [35] developed a novel microwave-assisted reverse micelle method (MARM) to produce thorium MOFs. The MOFs synthesized with MARM showed improved adsorption capacities for CO and CH_4 gases compared to those made with an ultrasonic-assisted reverse micelle method. In a previous study, UTSA-16 (Co) was synthesized by a microwave method [36], showing a 23% improved performance for CO_2 adsorption capacity as compared to solvothermal method due to uniform crystal structure. However, it still suffers from stability issue which causes reduced adsorption capacity and selectivity.

In this study, we developed a novel crystalline structure of UTSA-16 (Zn) composed of zinc and citric acid by using microwave irradiation in KOH solution. We investigated the effects of exchanging Zn for Co in UTSA-16 (Co) with regard to its physical properties, CO_2 separation performance, and stability to humid air and acid gases. The synthesis procedure was developed by changing reaction times to determine an optimal synthesis condition for the crystalline structure formation of UTSA-16 (Zn). CO_2 and N_2 adsorption capacities were measured using a volumetric method, thus producing adsorption selectivities. The synthesized samples with different reaction times were examined to determine crystalline morphology, pore size distribution, particle size, and thermal stability using X-ray diffraction (XRD), Brunauer–Emmett–Teller (BET), scanning electron microscopy (SEM), and thermogravimetric analysis (TGA), respectively. In addition, because combustion byproducts such as humid air and acid gases in flue gas break coordination bindings between metal and organic ligand, as a result reduced performance we investigated stability by exposing UTSA-16 (Zn) to humid air, SO_2, and NO_2 gases with concentrations between 15 and 25 ppm to prove its applicability in post-combustion CO_2 capture. Molecular diffusion of CO_2 and N_2 in UTSA-16 (Zn) was studied using a microporous model based on adsorption isotherms obtained from TGA measurements.

Experimental

Chemicals

All chemicals were purchased from Sigma–Aldrich and used without any further purification including zinc (II) acetate dihydrate (ACS reagent, ≥98.0%), citric acid (ACS reagent, ≥99.5%), deionized water, KOH (reagent grade, 90%), methanol (anhydrous, 99.8%), and diethyl ether (anhydrous, ≥99.7%) except ethanol (ACS reagent, ≥99.8%) which was obtained from Honeywell Chemicals. CO_2 and N_2 gases (>99.995%) were used for adsorption measurements.

Sample preparation

UTSA-16 (Zn) was synthesized by using a microwave irradiation power of 300 W at 90 °C for 1–6 h. $Zn(CH_3COO)_2 \cdot 2H_2O$ (1.5365 g), $C_6H_8O_7 \cdot H_2O$ (1.47 g), and KOH (1.17 g) were homogeneously mixed in 35 ml of solvent (H_2O:C_2H_5OH = 1:1 (V/V)). The solution was transferred into a glass reactor and tightly closed by a Teflon cap, and then kept in a microwave oven (Discover SP, CEM, USA). After microwave irradiation with different times, the white-colored samples were obtained by using centrifugation process (FLETA 5, Hanil, Korea) and washed with ethyl ether two times, methanol three times, and then immersed in methanol for solvent exchange by replenishing three times per day for 2–3 days. The powder product was separated from the solvent via centrifugation at 5000 rpm, and dried under vacuum for 2 h, followed by removal of excess solvent from the powder produced by heating at 90 °C for 6 h under vacuum.

Characterization

The crystallinity of the synthesized samples was examined from XRD diffraction patterns by using X'Pert Pro-MPD (PANalytical, Netherlands). Thermal stability was identified using TGA (Scinco TGA N1000) while heated to 800 °C at 5 °C per minute under N_2 gas flow at 50 mL/min. Fourier transform infrared (FTIR) spectra were measured using an FTIR 6300 spectrometer (JASCO, Japan) between 400 cm^{-1} and 4000 cm^{-1}. The particle size and powder morphologies of the UTSA-16 (Zn) samples, which were coated with gold–palladium, were examined based on microscope images taken from SEM instrument (Merlin compact, Carl Zeiss) under the condition of an accelerating voltage of 1 kV/10 kV and a current of 10 μA. BET surface area, pore volume, and pore size distribution of UTSA-16(Zn) samples were measured using a Quantachrome Instrument Autosorb iQ Station 1 under liquid nitrogen adsorption at 77 K.

Adsorption isotherm measurement

Adsorption capacities of CO_2 and N_2 for UTSA-16 (Zn) samples were measured based on a volumetric method by using BelSorp Mini II (MicrotracBEL, Japan) at different temperatures (298, 313, 323, 233, 343 and 353 K) under 0–1 bar where temperatures were controlled using a water-circulating container connected to a temperature controller with an accuracy of ±0.01 °C. CO_2, N_2, and He gases with ultrahigh purity grade (>99.995%) were used. Helium gas was used to determine the free space of the sample holder in the volumetric apparatus. Samples were degassed by heating at 90 °C for 12 h under vacuum before each measurement.

Stability to humid air and acid gases

The stability of UTSA-16 (Zn) was investigated by comparing adsorption capacities and XRD patterns before and after separate exposure to humid air and SO_2 and NO_2 gases. The samples were conditioned to humid air with a relative humidity of 80% and then conditioned to SO_2 (15 ppm) and NO_2 (10 ppm) with 80% relative humidity at room temperature, respectively, each for 2 days. The acid gases with controlled concentrations were produced using salt solutions with different pH in aqueous solution, temperatures, and flow rate of carrier gas [37]. Between each exposure, we measured adsorption capacities and X-ray diffraction patterns for UTSA-16 (Zn) samples evacuated at 90 °C under vacuum for 12 h. pH 3.7 $NaHSO_3$ aqueous solution (500 μg/ml) was used at 45 °C to generate 15 ppm SO_2 gas. Airflow (200 ml/min) was used to deliver SO_2 gas from a reactor to a desiccator where UTSA-16 (Zn) samples were placed under 80% relative humidity and prepared using a saturated NaCl aqueous solution. pH 3 $NaNO_2$ aqueous solution (800 μg/ml) at 45 °C was used to generate 10 ppm NO_2 gas. Airflow (100 ml/min) was used to transfer NO_2 gas from a reactor to a desiccator. To generate 25 ppm SO_2 and NO_2, the preparation conditions were similar except that the air flow was 100 ml/min for SO_2 and 50 ml/min for NO_2. Concentrations of SO_2 and NO_2 were identified using Drager-Tubes (Drager, Germany). The reaction mechanism of SO_2 is shown below.

$NaHSO_3 \rightarrow Na^+ + HSO_3^-$

$HSO_3^- \rightarrow H^+ + H_2SO_3$

$H_2SO_3 \rightarrow H_2O + SO_2$

Results and discussion

Structural characterization and thermal stability

The structural properties of UTSA-16 (Zn) with different reaction times were measured from liquid N_2 adsorption isotherms (Fig. 1) at 77 K using a Quantachrome Instrument Autosorb iQ Station 1. The initial large increase at low pressure ($P/P_0 < 0.1$) is a notable behavior of the type I isotherms caused by a micropore structure of the UTSA-16 (Zn). The surface areas and pore volumes in Table 1 increased from 475.38 m^2/g to 786.61 m^2/g and from 0.5038 cm^3/g to 0.7875 cm^3/g in the reaction time from 1 h to 4 h, respectively. As the reaction time increased above 4 h, the surface area and pore volume decreased showing maximum values at 4 h, possibly due to the competing reaction of unreacted Zn clusters with organic ligands. 4h-UTSA-16 (Zn) was selected for pore size distribution investigation from the N_2 adsorption–desorption isotherms. When Co was replaced with Zn in UTSA-16, the majority of the pores (Fig. 2) were in the range of 0.3–1.79 nm for 4h-UTSA-16 (Zn), a larger value as compared to the pore size distribution of UTSA-16 (Co) (0.3–1.45 nm). The surface area of 4h-UTSA-16 (Zn) was decreased in comparison to the surface area of 4h-UTSA-16 (Co), while the total pore volume was increased compared to the UTSA-16 (Co) [36]. The specific surface area is mainly affected by the atomic weight of the metal in MOF framework in the case of metal replacement [38]. A

similar trend was observed in other MOFs [38] such as Mg/DOBDC (1495 m^2/g), Co/DOBDC (1080 m^2/g), Ni/DOBDC (1070 m^2/g) and Zn/DOBDC (816 m^2/g) where specific surface area was decreased with increase in atomic weight of metal from Mg to Zn in MOFs.

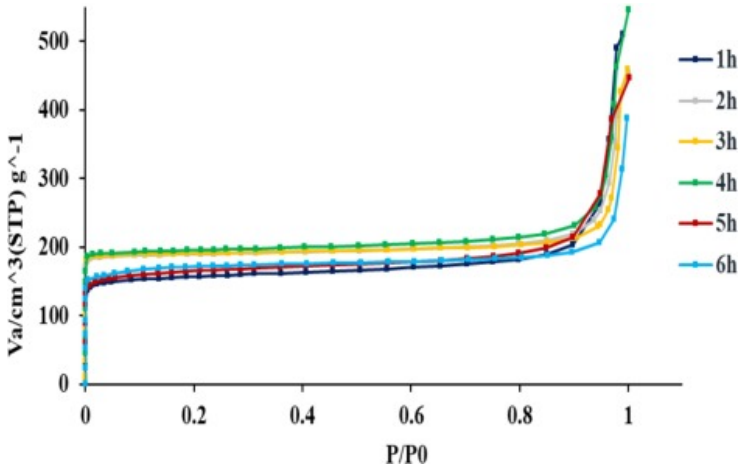

Download : Download high-res image (128KB) Download : Download full-size image

Fig. 1. N_2 adsorption isotherm of microwave-assisted synthesized UTSA-16 (Zn) with different reaction times at 77 K.

Table 1. Specific surface area and pore volume of UTSA-16 (Zn).

Adsorbents	Specific surface area (m^2/g)	Total pore volume (cm^3/g)
1h-UTSA-16 (Zn)	475.38	0.5038
2h-UTSA-16 (Zn)	577.35	0.7499
3h-UTSA-16 (Zn)	580.91	0.7824
4h-UTSA-16 (Zn)	786.61	0.7875
5h-UTSA-16 (Zn)	514.96	0.6753
6h-UTSA-16 (Zn)	500.19	0.6553

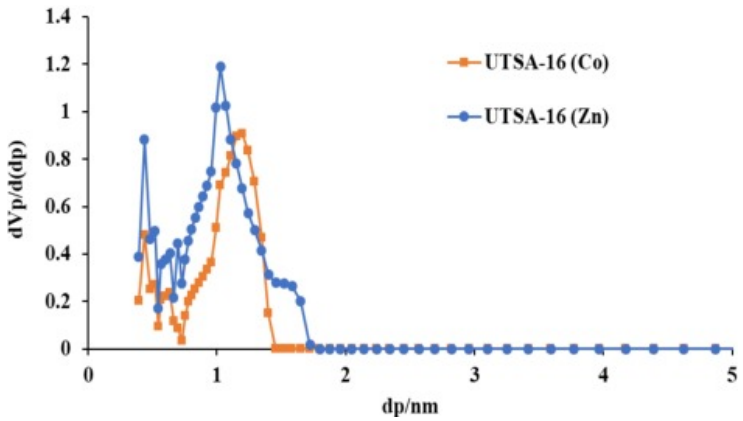

Download : Download high-res image (107KB) Download : Download full-size image

FEEDBACK

Fig. 2. Pore size distribution graphs of 4h-UTSA-16 (Zn) and 4h- UTSA-16 (Co) calculated using the NLDFT method.

The morphology and the powder size of samples (Fig. 3) are affected by reaction time as it increases from 1 to 6 h. The particles of 1h-UTSA-16 (Zn) and 2h-UTSA-16 (Zn) showed a granular aspect. As reaction time went above 3 h, polyhedron structures were observed with well-defined faces and edges. The size of UTSA-16 (Zn) particle increased from 0.18 to 0.27 μm with continuous nucleation by attaching small granular particles on the surface of the particle (Fig. 3(e)) as measured with Image J software (NIH, USA).

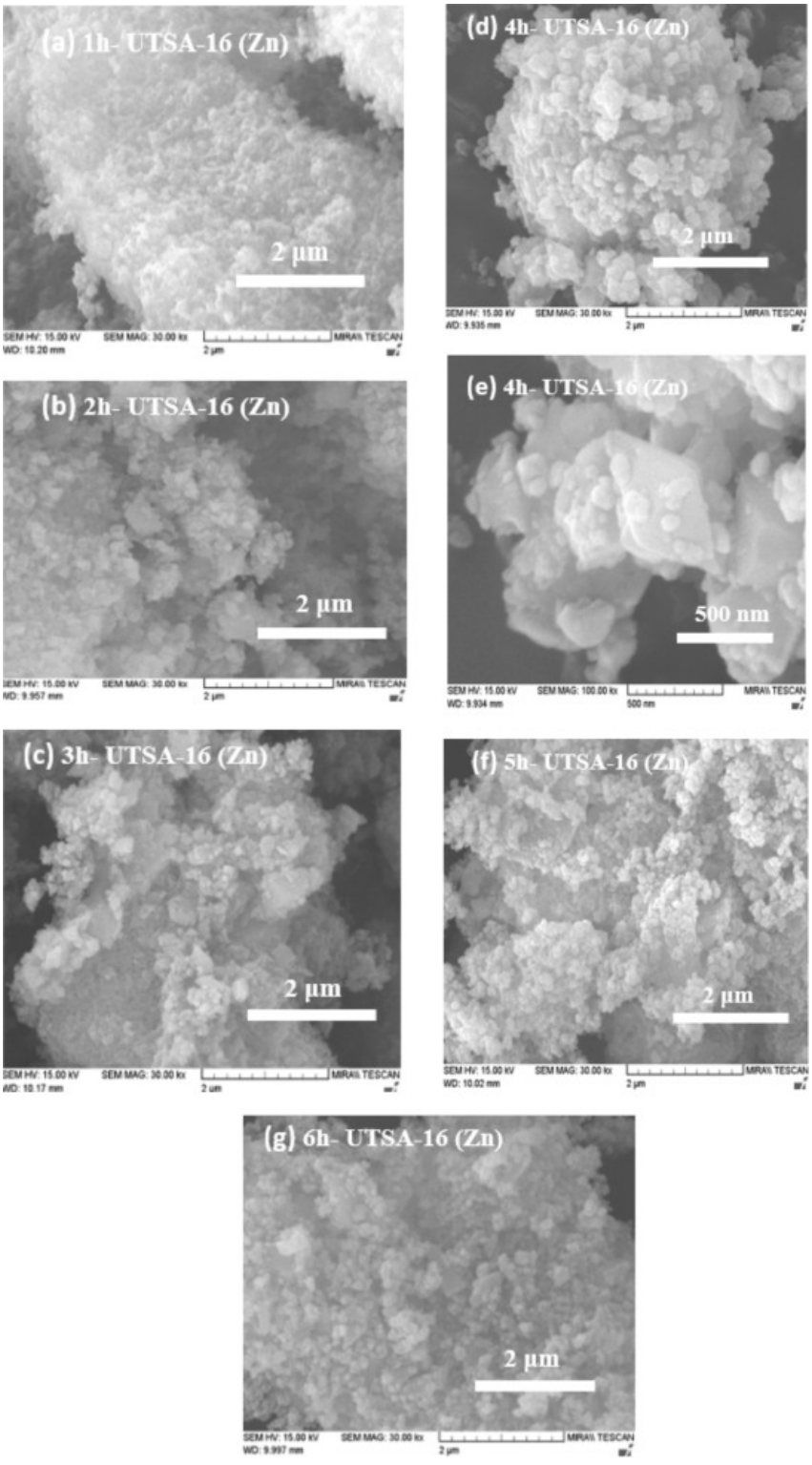

FEEDBACK

Fig. 3. SEM images of UTSA-16 (Zn) samples with reaction time increase of (a) 1 h, (b) 2 h, (c) 3 h, (d) 4 h, (e) 4 (enlarged), (f) 5 h, and (g) 6 h.

Thermal stabilities of UTSA-16 (Zn) samples were evaluated by using TGA with a heating rate of 20 °C/min (Fig. 4). The first drop in weight between 100 and 170 °C corresponds to the evaporation of adsorbed water and impurities from the samples. After the first drop, all samples were stable up 320 °C. Interestingly, the 1 h sample showed a 35% weight loss from 320 to 440 °C and 4% further decrease up to 470 °C. However, samples with reaction times over 3 h showed a 32% loss from 320 to 480 °C, suggesting that the samples prepared with a small reaction time are not stable upon heating which results in more loss of organic ligands and collapse of the crystal structure. The TGA results correlate well to the thermal analysis data (Fig. S1 in supporting information) obtained by using a differential scanning calorimetry (DSC, Q600 SDT TA Instruments, USA). For 4h-UTSA-16 (Zn) sample, three endothermic peaks were discovered at 90–150 °C for dehydration, 300–315 °C and 330–360 °C for decomposition.

The crystal structure of UTSA-16 (Zn) was examined using XRD measurements (Fig. 5). The main diffraction peaks were observed at 11.3, 13.8, 21.3, 28.4, which are identical to the diffraction data of UTSA-16 (Co) [36]. The strong and sharp shapes of main peaks prove a highly ordered crystalline structure for the UTSA-16 (Zn). The similarity of the XRD patterns indicates that the substituted Zn metal did not affect the characteristic crystal structure of UTSA-16, which was composed of Co.

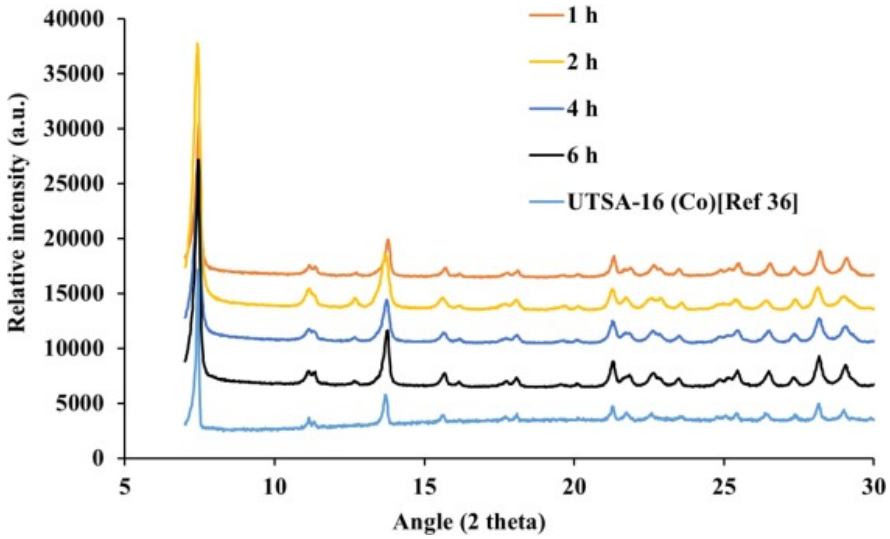

Fig. 5. XRD patterns of UTSA-16 (Zn) with reaction time increase (1–6 h).

CO_2 and N_2 adsorption capacity measurements

To examine the CO_2 capture performance as a function of reaction time, CO_2 and N_2 adsorption capacities (Fig. 6) were measured separately at 298 K under a pressure range of 0–1 bar using a volumetric method. The 1h-UTSA-16 (Zn) showed the lowest CO_2 capacity because of the incomplete crystal structure of UTSA-16 (Zn), consistent with it having the lowest surface area (Table 1). The CO_2 capacity for the 1 h sample was much lower than the 6 h sample (35% capacity of 6 h sample at 1 bar), although there was only a small difference in surface area (475.38 m^2/g for 1 h, 500.19 m^2/g for 6 h), highlighting the importance of an optimized reaction time for capture performance. CO_2 adsorption capacities increased with a reaction time increase, showing a maximum capacity of 4.71 mmol/g at a reaction time of 4 h. This well corresponds to the largest surface area and pore volume (Table 1) provided by the complete crystalline structure for the reaction time of 4 h. Once the reaction ti

it showed decreased CO_2 capacities by 30–35% compared to that of 4h-UTSA-16 (Zn). On the contrary, there was no increasing trend in N_2 adsorption as the reaction time increased, resulting in enhanced CO_2/N_2 adsorption selectivity concurrent with increased reaction times. The adsorption selectivity (Fig. 7) of UTSA-16 (Zn) gradually increased to 118 as reaction time increased and then decreased after 4 h, 4h-UTSA-16 (Zn) showed the highest selectivity (118) among other MOFs (6 for CuDABCO [39], 8 for ZIF-8 [40], 12 for MIL-101 (Cr) [41], 18 for MOF-5 [42], 16.5 for MOF-177 [42] and 104 for UTSA-16 (Co) [36]).

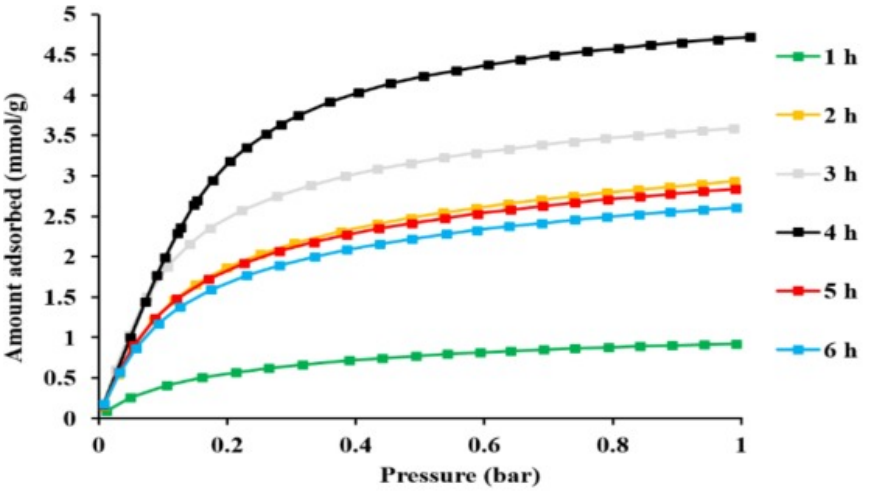

a) CO_2 adsorption

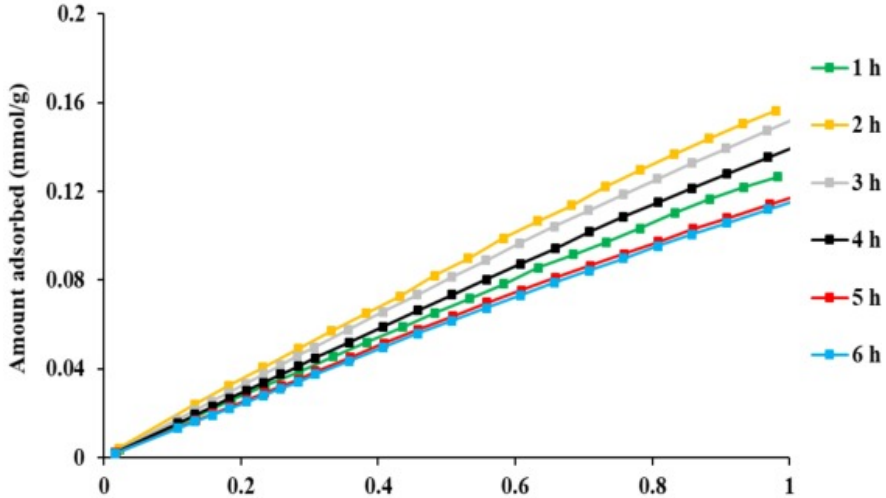

b) N_2 adsorption

Download : Download high-res image (361KB) Download : Download full-size image

Fig. 6. CO_2 (a) and N_2 (b) adsorption capacities at 298 K of UTSA-16 (Zn) prepared with different reaction times.

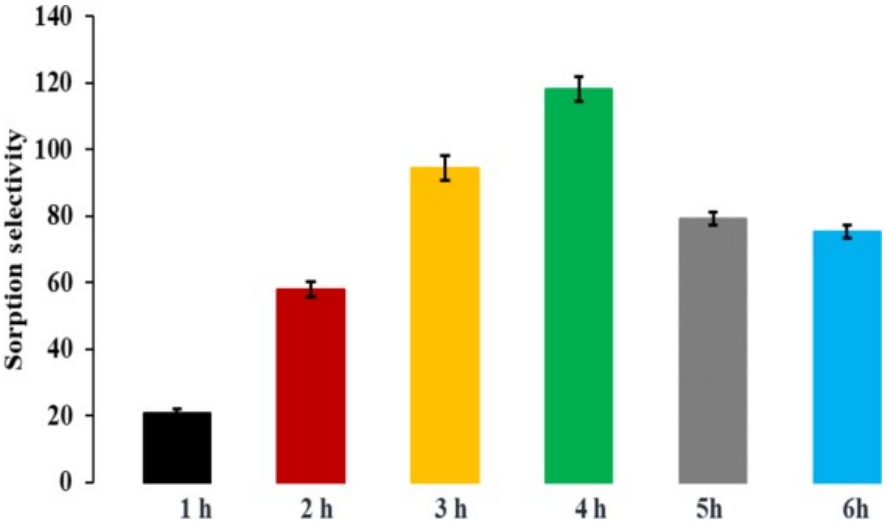

Download : Download high-res image (120KB) Download : Download full-size image

Fig. 7. CO_2/N_2 selectivities for UTSA-16 (Zn) prepared with different reaction times. Error bars represent standard deviation ($n = 3$).

Furthermore, the CO_2 adsorption capacity of UTSA-16 (Zn) (4.71 mmol/g) was higher than other composite adsorbents and MOF fibers such as polyethyleneimine (PEI)@MIL-101(Cr,Mg) (3.04 mmol/g) [43], ZIF-8 PAN fiber (0.8 mmol/g), HKUST-1 PAN fiber (2.55 mmol/g) [44], amine@MCM-48 (2.05 mmol/g) [45], graphite oxide (GO)@MOF-505 (3.94 mmol/g) [46], HKUST-1 monolith (2.8 mmol/g) [47], 5A zeolite@ZIF-8 composite (2.97 mmol/g) [48] at 298 K and 1 bar. Adsorption selectivity of UTSA-16 (Zn) (118) for CO_2/N_2 was even much higher than other composite MOFs such as PEI@ZIF-8 (25.4) [49], 5A zeolite@ZIF-8 composite (30) [48] and PEI@PAN/ZIF-8 (54) [44].

Stability analysis to humid air and acid gases

The stability of 4h-UTSA-16 (Zn) in flue gas impurities was verified by comparing adsorption capacities and XRD patterns before and after the samples were conditioned to humid air and acid gases (Fig. 8). The XRD patterns for samples conditioned to humid air, SO_2, and NO_2 look identical, even with regard to small details. UTSA-16 (Co), however, showed small changes in peak position and peak intensity after the exposures [36].

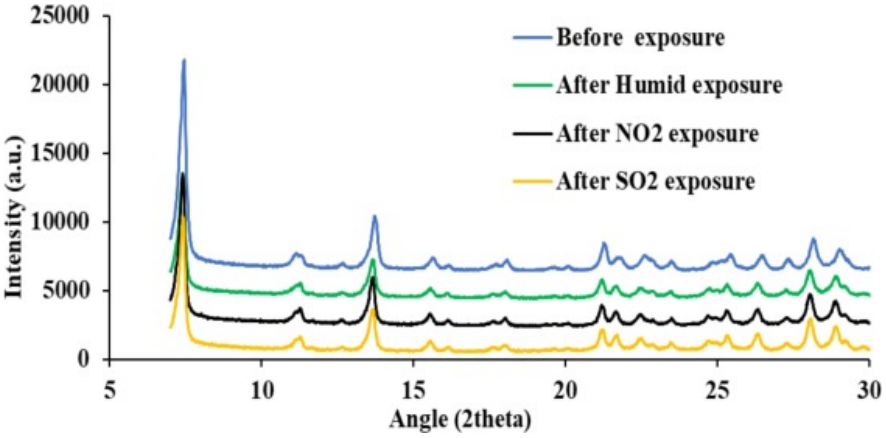

Download : Download high-res image (209KB) Download : Download full-size image

Fig. 8. XRD patterns of 4h-UTSA-16 (Zn) after exposure to impurities.

FEEDBACK

The adsorption capacities were examined before and after each exposure to humid air, SO_2, and NO_2 gases to determine any effects of impurities on adsorption performance, even though the crystal structure had remained intact. The exposed samples were cleaned by heating at 90 °C under vacuum for 12 h before each adsorption experiment. There were negligible changes in CO_2 adsorption capacities when conditioned to SO_2 (15 ppm) and NO_2 (10 ppm) (Fig. S2 in supporting information), whereas UTSA-16 (Co) showed a 28–40% decrease, suggesting a significantly improved stability with metal exchange to Zn [36]. The adsorption selectivities of 4h–UTSA-16 (Zn), where the selectivity is defined as the ratio of CO_2 adsorption capacity at 0.15 bar to the N_2 adsorption capacity at 0.85 bar, giving a normalized value at given pressures (Fig. S3 in supporting information), decreased by 6% after humid air and NO_2 and by 17% after SO_2 exposure (Fig. 9). These values are still higher than others reported in the literature values, even after exposure (22.5 for ZIF-79 [50], 20 for ZIF-69 [50], 19.5 for ZIF-68 [50], 50 for ZIF-78 [51], and 38 for Ni/DOBDC [52]).

We further investigated the stability performance for UTSA-16 (Zn) and UTSA-16 (Co) at increased concentrations of acid gases (25 ppm each for SO_2 and NO_2). CO_2 adsorption capacities for UTSA-16 (Co) at 298 K and 1 bar were decreased by 6% and 47% after exposure to NO_2 and SO_2, respectively (Fig. 10(a)), while capacities for UTSA-16 (Zn) were decreased only by 6% and 10%, respectively (Fig. 10(b)). In addition, there were relatively small decreases in the selectivities after exposure for UTSA-16 (Zn) compared to UTSA-16 (Co) (Fig. S4 in supporting information).

Diffusivity estimation and temperature effect on adsorption

For the adsorption separation processes, the mobility of adsorbed gas molecules into porous adsorbents is an important aspect as well as adsorption capacity. To identify the effects of humid air and acid gases on the mobility of CO_2 and N_2 molecules, molecular diffusion coefficients of the gases in 4h-UTSA-16 (Zn) were investigated. Ruthven [53] described a typical micropore diffusion model and it was used to process the CO_2 and N_2 kinetic data to estimate the intracrystalline diffusivities of CO_2 and N_2 in 4h-UTSA-16 (Zn) based on adsorption amounts of CO_2 and N_2 with time increase at 298 K and 1 bar by TGA. The ratio of adsorption uptake (m_t/m_∞) can be associated with diffusion time using Eq. (1).

$$1 - \frac{m_t}{m_{max}} = \frac{6}{\pi^2}\exp\frac{-\pi^2 D_c t}{r_c^2} \quad (1)$$

where, t is the diffusion time (s), D_c is the intracrystalline diffusivity (cm^2/s), m_{max} is the limit of adsorption amount per unit mass (mmol/g), m_t is the adsorption capacity per unit mass at time t (mmol/g), and r_c is the radius of an adsorbent powder (cm).

The diffusion time constants (D_c/r_c^2, s^{-1}) were evaluated from the relation between the linear plot of ln (1 – (m_t/m_∞)) and time. The intracrystalline diffusivity, D_c, was then evaluated from the diffusion time constant. The radius of a crystal particle was measured using ImageJ software [54] based on the SEM images of the 4h-UTSA-16 (Zn) samples. The average radius of particles for 4h-UTSA-16 (Zn) was 0.24 μm (Fig. 3(d)). The CO_2 diffusivities (Table 2) decreased after each exposure, showing that molecular diffusion was hindered regardless of the negligible changes in crystallinity and adsorption capacity. A similar decrease in diffusivity was observed for MIL-101(Cr, Mg) impregnated with polyethyleneimine after exposure to humid air and acid gas [43]. The CO_2 diffusivities for UTSA-16 (Zn) were similar to those reported for UTSA-16 (Co) [36], which were lower than reported diffusivities for other MOFs (1.50×10^{-10}, 1.60×10^{-8}, 1.70×10^{-8}, 3.00×10^{-8}, and 7.40×10^{-9} cm^2/s for ZIF-90, Co-NIC, Ni-HF, Zn/Co-BTEC, and Zn-TTC) [55].

Table 2. CO_2 and N_2 diffusion coefficients of 4h-UTSA-16 (Zn) after exposure to impurities.

Gas	Intracrystalline diffusivity (D_c), cm^2			
	Before exposure	After humid air exposure	After NO_2 exposure	After SO_2 exposure
N_2	9.87×10^{-17}	4.73×10^{-17}	2.86×10^{-17}	1.46×10^{-17}
CO_2	2.28×10^{-13}	1.81×10^{-13}	1.69×10^{-13}	1.52×10^{-13}

To investigate temperature effects on adsorption capacities, adsorption capacities were measured as temperature was increased from 298 to 338 K. The adsorption amounts were gradually decreased with increasing temperature (Fig. 11), while CO_2/N_2 sorption selectivities were decreased until 318 K, and then increased with higher temperatures (Fig. 12), showing the minimum selectivity of 78 at 318 K which is still higher than most of the selectivities reported in the literature (20–25) for Cu-BTC MOF [56], (19) for zeolite 4A [57], and (18) for Zeolite 13X [57] under the same conditions. This is presumably due to the relatively small decrease in CO_2 capacity compared with N_2 capacity at increased temperatures.

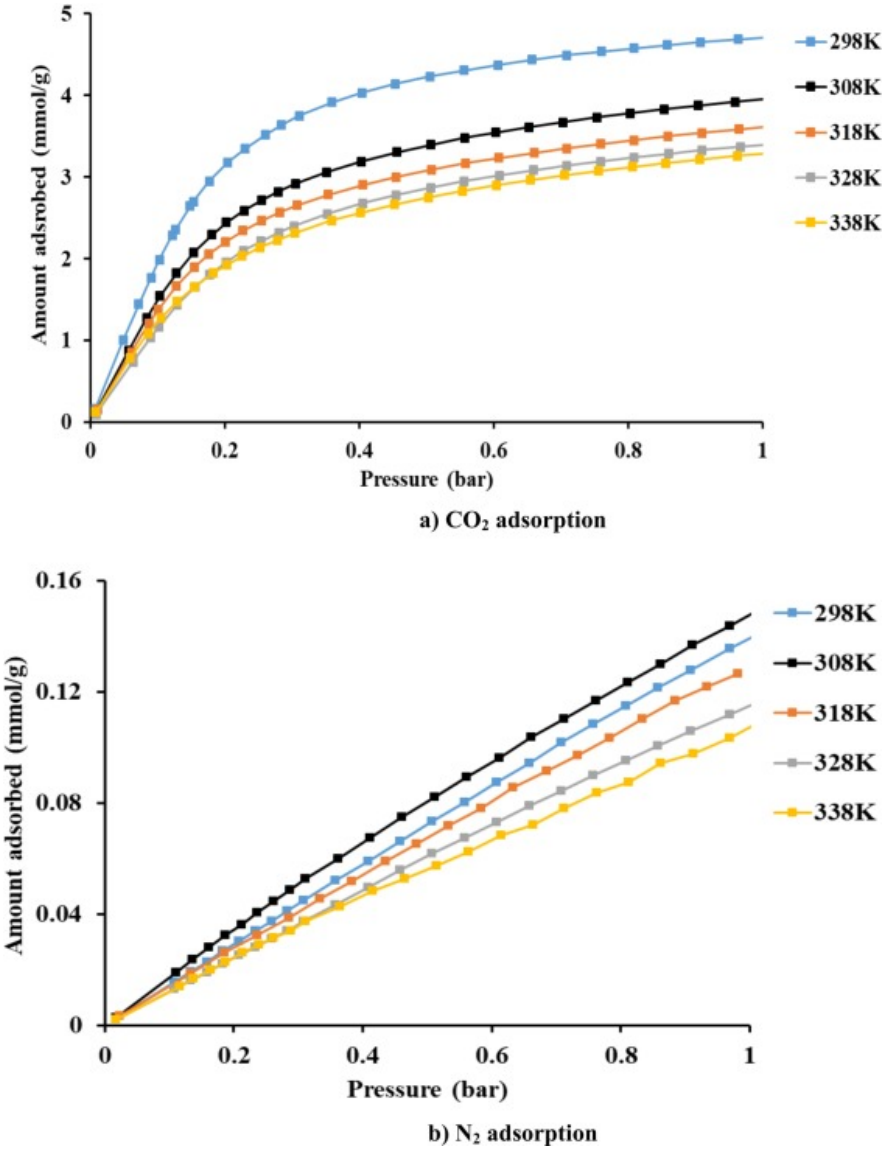

Download : Download high-res image (361KB) Download : Download full-size image

Fig. 11. CO_2 (a) and N_2 (b) adsorption isotherms of 4h-UTSA-16 (Zn) at different temperatures.

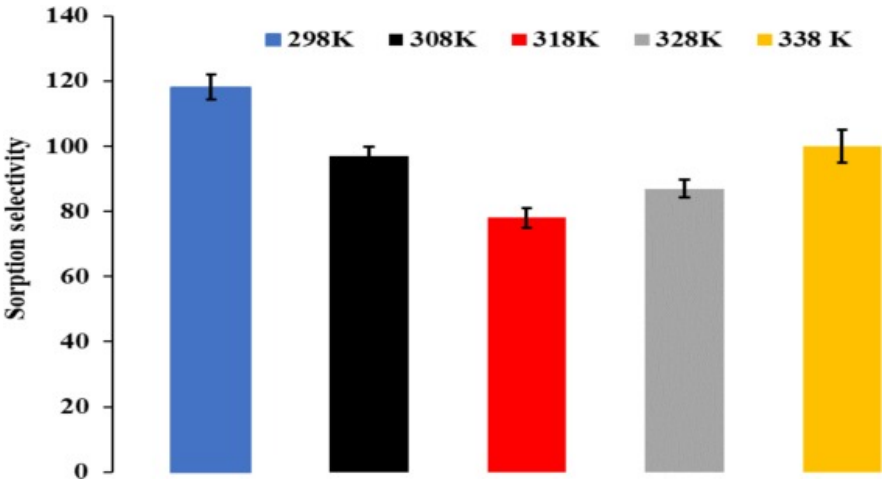

Download : Download high-res image (135KB) Download : Download full-size image

Fig. 12. CO_2/N_2 selectivities for 4h-UTSA-16 (Zn) at different temperatures. Error bars represent the standard deviation ($n = 3$).

FTIR analysis after exposure to SO_2 and NO_2

FT-IR spectra for 4h-UTSA-16 (Zn) were measured to reveal the molecular interactions or bonding formations after exposure to NO_2 and SO_2 (Fig. 13). The samples were degassed by evacuating at 90 °C for 12 h after separate exposure of SO_2 and NO_2 each for 2 days at 80% relative humidity to evacuate the samples from unreacted SO_2 and NO_2 in the pores. The FTIR spectra after exposure to SO_2 at 15 and 25 ppm clearly show a new peak at 650 cm^{-1} due to S–O stretching vibrations [36]. However, no band appeared at 1345–1385 cm^{-1} which would have indicated N–O stretching after exposure to NO_2 at 10 and 25 ppm. This discrepancy indicates that there was no formation or functionality by NO_2 gas adsorption [58]. Interestingly, there was less of a decrease in CO_2 adsorption capacity for UTSA-16 (Zn) than for UTSA-16 (Co) (Fig. 10(a)), despite the sulfate formation after SO_2 exposure, highlighting the improved stability of UTSA-16 (Zn). Correspondingly, CO_2 adsorption analysis (Fig. 10(b)) also showed that adsorption capacities were not affected by exposure to humid air and acid gases. However, adsorption capacities were reduced via sulfate formation for UTSA-16 (Co) after SO_2 exposure, due to its low stability [36]. The two peaks at 1395 and 1574 cm^{-1} indicate the symmetric and antisymmetric stretching vibrations of carboxylic functionalities in the UTSA-16 (Zn), respectively [59].

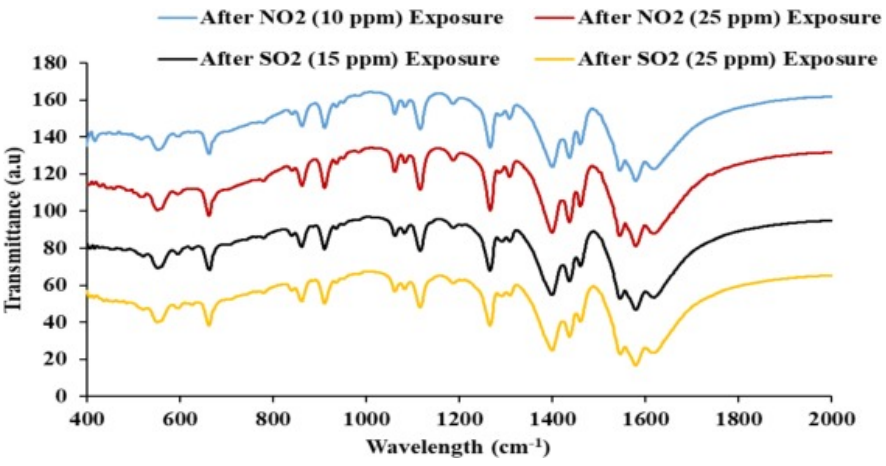

Download : Download high-res image (255KB) Download : Download full-size image

Fig. 13. FTIR spectra of 4h-UTSA-16 (Zn) after NO_2 and SO_2 exposure with degassing.

Cyclic performance of UTSA-16 (Zn) CO_2 capture

Stable adsorption performance during cyclic operations is important for practical applications in separation processes with adsorbents. Here we investigated the cyclic ability of UTSA-16 (Zn) by performing five consecutive cycles of CO_2 adsorption using a volumetric method at 298 K and 338 K (Fig. 14). From CO_2 adsorption isotherms (Fig. S5 in supporting information), the maximum adsorption capacities at 1 bar are presented which show a constant performance in adsorption at both temperatures.

Analysis of MOF production cost

The synthesis cost of MOF is all the time a critical topic to study for practical applications. The total cost for 1 g of each MOF production was estimated based on the required amounts of the metal precursor and organic linker, and the amount of produced MOF (Table S1 in supporting information). The unit cost for each reactant was obtained from Sigma–Aldrich. Due to the relatively low cost (0.21 USD/g) of Zn precursor, UTSA-16 (Zn) showed the smallest production cost (0.91 USD/g) for 1 g of MOF among UTSA-16 (Co) (3.12 USD/g) [36], HKUST-1 (1.96 USD/g) [60], MOF-199 (3.85 USD/g) [61], [62], MOF-74 (64.23 USD/g) [61] MOF-5 (2.31 USD/g) [61], [63], MIL-101 (1.97 USD/g)[64], [65], [66] UiO-66 (32.11 USD/g) [67] and IRMOF-0 (23.31 USD/g) [61] (Fig. 15), presenting additional advantage of reduced production cost as well as improvement in stability and selectivity when Co was replaced with Zn in the UTSA-16 framework.

For a further economic analysis regarding CO_2 capture performance, CO_2 capture capacities at 1 bar and 298 K and adsorption selectivities at 298 K were divided by the production cost for 1 g of each MOF. The CO_2 adsorption capacity and selectivity for UTSA-16 (Zn) per unit cost were superior to other MOFs (Fig. 16), showing the practical applicability due to the outstanding capacity, selectivity, stability, and low cost.

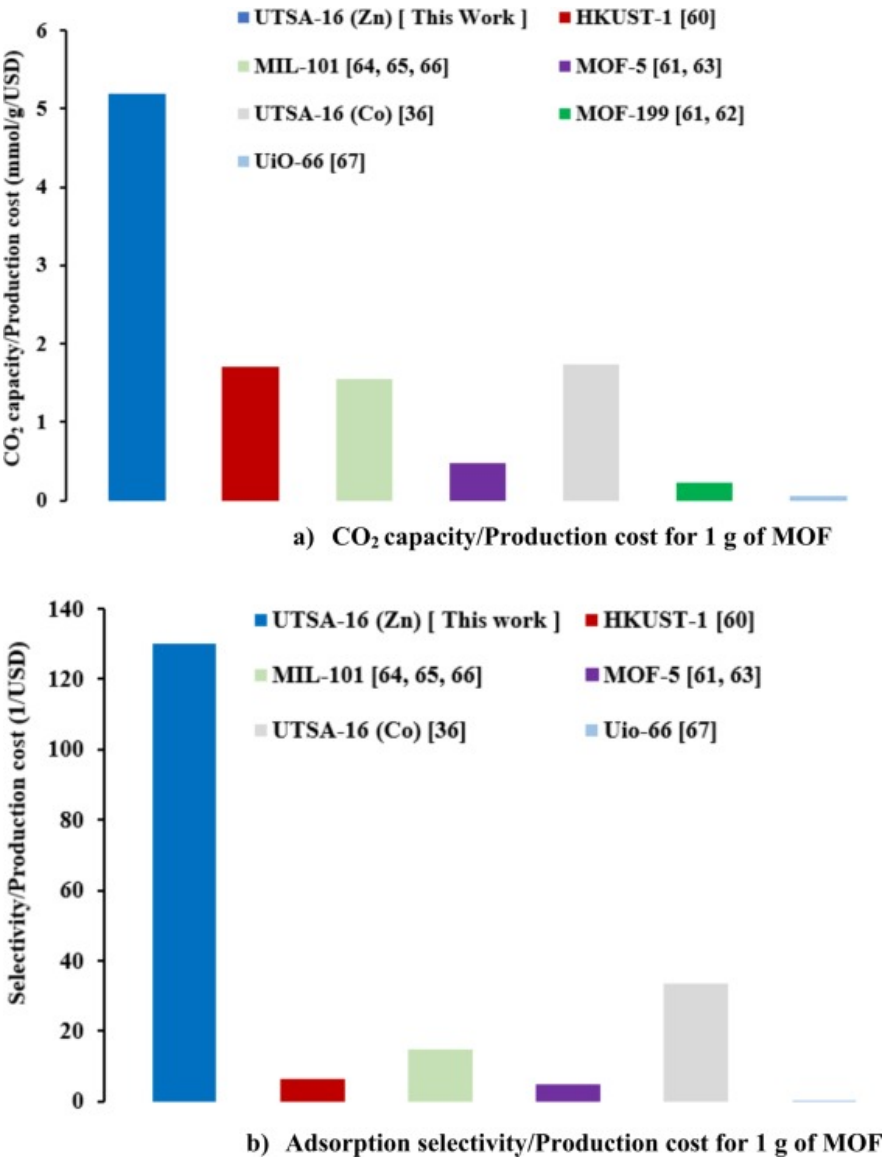

Download : Download high-res image (316KB) Download : Download full-size image

Fig. 16. CO_2 adsorption capacity (a) and adsorption selectivity (b) normalized by MOF production cost for 1 g.

Conclusion

UTSA-16 (Zn) has been successfully produced by replacing Co metal with Zn using a microwave method while maintaining the original framework of UTSA-16 (Co). XRD spectra confirmed that all diffraction peaks of UTSA-16 (Zn) were identical to the parent UTSA-16 (Co), suggesting that the Zn replacement does not affect the original crystallinity of UTSA-16 (Co). According to the study on reaction time for the synthesis, it was revealed that the synthesis time of 4 h is optimal for high surface area, large pore volume, and maximum CO_2 capture performance. The surface area (786.61 m^2/g) of UTSA-16 (Zn) was slightly lower than that of UTSA-16 (Co) (804.2 m^2/g), while total pore volume of UTSA-16 (Zn) (0.788 cm^3/g) was increased more than twice as compared to UTSA-16 (Co) (0.353 cm^3/g). UTSA-16 (Zn) with an optimized synthesis time of 4 h showed a noticeable improvement in stability for adsorption capacity after exposure to SO_2 and NO_2 gases compared to the parent UTSA-16 (Co) while possessing the high CO_2 adsorption of the parent UTSA-16 (Co). Furthermore, the CO_2/N_2 adsorption selectivity of UTSA-16 (Zn) showed a 13% increase (from 104 to 118) over the UTSA-16 (Co), which is an outstanding value as compared to other MOFs and composites with PEI (21 for MOF-591, 27 for MOF-592 [68], 12 for MIL-101 (Cr) [41], 18 for MOF-5 [42]). The developed UTSA-16 (Zn) can be a strong candidate for CO_2 capture in flue gas because of the enhanced stability,

adsorption capacity, and selectivity. The lowest production cost of UTSA-16 (Zn) among other MOFs further highlights that the UTSA-16 (Zn) is one of the best MOF adsorbents for post-combustion CO_2 capture reported so far. In the near future, pellets will be made exclusively from UTSA-16 (Zn) or as a composite with other low-cost porous material such as activated carbon for a practical application.

Conflicts of interest

The authors declare no conflicts of interest.

Acknowledgements

This research was supported by the Basic Science Research Program through the National Research Foundation of Korea (NRF) grant funded by the Korea government (MSIT) (#NRF-2017R1C1B1002851) and the Cooperative R&D between Industry, Academy, and Research Institute funded Korea Ministry of SMEs and Startups in 2019 (Grant No. S2652595).

Appendix A. Supplementary data

The following are the supplementary data to this article:

Download : **Download Word document (437KB)**

Recommended articles Citing articles (1)

References

[1] M. Wise, K. Calvin, A. Thomson, L. Clarke, B. Bond-Lamberty, R. Sands, S.J. Smith, A. Janetos, J. Edmonds
Science, 324 (2009), pp. 1183-1186
CrossRef View Record in Scopus

[2] R. Quadrelli, S. Peterson
Energy Policy, 35 (2007), pp. 5938-5952
Article Download PDF View Record in Scopus

[3] R. Littel, G. Versteeg, W.P.M. Van Swaaij
Chem. Eng. Sci., 46 (1991), pp. 3308-3313
Article Download PDF View Record in Scopus

[4] S. Choi, J.H. Drese, C.W. Jones
ChemSusChem, 2 (2009), pp. 796-854
CrossRef View Record in Scopus

[5] A. Sayari, Y. Belmabkhout, R. Serna-Guerrero
Chem. Eng. J, 171 (2011), pp. 760-774
Article Download PDF View Record in Scopus

[6] K. Sumida, D.L. Rogow, J.A. Mason, T.M. McDonald, E.D. Bloch, Z.R. Herm, T.-H. Bae, J.R. Long
Chem. Rev., 112 (2011), pp. 724-781
View Record in Scopus

[7] M.R. Hudson, W.L. Queen, J.A. Mason, D.W. Fickel, R.F. Lobo, C.M. Brown
J. Am. Chem. Soc., 134 (2012), pp. 1970-1973
CrossRef View Record in Scopus

[8] S. Regati, Y. He, M. Thimmaiah, P. Li, S. Xiang, B. Chen, J.C.-G. Zhao

Chem. Commun., 49 (2013), pp. 9836-9838
CrossRef View Record in Scopus

[9] J. Liu, L. Chen, H. Cui, J. Zhang, L. Zhang, C.-Y. Su
Chem. Soc. Rev., 43 (2014), pp. 6011-6061
View Record in Scopus

[10] I. Imaz, M. Rubio-Martínez, J. An, I. Sole-Font, N.L. Rosi, D. Maspoch
Chem. Commun., 47 (2011), pp. 7287-7302
CrossRef View Record in Scopus

[11] P. Horcajada, R. Gref, T. Baati, P.K. Allan, G. Maurin, P. Couvreur, G. Ferey, R.E. Morris, C. Serre
Chem. Rev., 112 (2011), pp. 1232-1268
View Record in Scopus

[12] M. Allendorf, C. Bauer, R. Bhakta, R. Houk
Chem. Soc. Rev., 38 (2009), pp. 1330-1352
CrossRef View Record in Scopus

[13] M. Clemente-León, E. Coronado, C. Martí-Gastaldo, F.M. Romero
Chem. Soc. Rev., 40 (2011), pp. 473-497
CrossRef View Record in Scopus

[14] Y. Jiao, C.R. Morelock, N.C. Burtch, W.P. Mounfield III, J.T. Hungerford, K.S. Walton
Ind. Eng. Chem. Res., 54 (2015), pp. 12408-12414
CrossRef View Record in Scopus

[15] J.A. Botas, G. Calleja, M. Sánchez-Sánchez, M.G. Orcajo
Langmuir, 26 (2010), pp. 5300-5303
CrossRef View Record in Scopus

[16] Y.-S. Bae, B.G. Hauser, O.K. Farha, J.T. Hupp, R.Q. Snurr
Microporous Mesoporous Mater., 141 (2011), pp. 231-235
Article Download PDF View Record in Scopus

[17] Y. Cao, Y. Zhao, F. Song, Q. Zhong
J. Energy Chem., 23 (2014), pp. 468-474
Article Download PDF View Record in Scopus

[18] Z. Wei, W. Lu, H.-L. Jiang, H.-C. Zhou
Inorg. Chem., 52 (2013), pp. 1164-1166
CrossRef View Record in Scopus

[19] W. Lu, Z. Wei, Z.-Y. Gu, T.-F. Liu, J. Park, J. Park, J. Tian, M. Zhang, Q. Zhang, T. Gentle III
Chem. Soc. Rev., 43 (2014), pp. 5561-5593
CrossRef View Record in Scopus

[20] N.C. Burtch, H. Jasuja, K.S. Walton
Chem. Rev., 114 (2014), pp. 10575-10612
CrossRef View Record in Scopus

[21] H. Deng, C.J. Doonan, H. Furukawa, R.B. Ferreira, J. Towne, C.B. Knobler, B. Wang, O.M. Yaghi
Science, 327 (2010), pp. 846-850
CrossRef View Record in Scopus

[22] V. Safarifard, S. Rodríguez-Hermida, V. Guillerm, I. Imaz, M. Bigdeli, A. Azhdari Tehrani, J. Juanhuix, A. Morsali, M.E. Casco, J. Silvestre-Albero

Cryst. Growth Des., 16 (2016), pp. 6016-6023
CrossRef View Record in Scopus

[23] N. Stock, S. Biswas
Chem. Rev., 112 (2011), pp. 933-969
View Record in Scopus

[24] Y.-R. Lee, J. Kim, W.-S. Ahn
Korean J. Chem. Eng., 30 (2013), pp. 1667-1680
CrossRef View Record in Scopus

[25] K. Sumida, D.L. Rogow, J.A. Mason, T.M. McDonald, E.D. Bloch, Z.R. Herm, T.-H. Bae, J.R. Long
Chem. Rev., 112 (2012), pp. 724-781
CrossRef View Record in Scopus

[26] M.Y. Masoomi, K.C. Stylianou, A. Morsali, P. Retailleau, D. Maspoch
Cryst. Growth Des., 14 (2014), pp. 2092-2096
CrossRef View Record in Scopus

[27] H. He, L. Hashemi, M.-L. Hu, A. Morsali
Coord. Chem. Rev., 376 (2018), pp. 319-347
Article Download PDF View Record in Scopus

[28] Z. Ni, R.I. Masel
J. Am. Chem. Soc., 128 (2006), pp. 12394-12395
CrossRef View Record in Scopus

[29] J. Klinowski, F.A.A. Paz, P. Silva, J. Rocha
Dalton Trans., 40 (2011), pp. 321-330
CrossRef View Record in Scopus

[30] N.A. Khan, E. Haque, S.H. Jhung
Phys. Chem. Chem. Phys., 12 (2010), pp. 2625-2631
CrossRef View Record in Scopus

[31] G.H. Albuquerque, G.S. Herman
Cryst. Growth Des., 17 (2016), pp. 156-162

[32] C. Chen, X. Feng, Q. Zhu, R. Dong, R. Yang, Y. Cheng, C. He
Inorg. Chem., 58 (2019), pp. 2717-2728
CrossRef View Record in Scopus

[33] S.H. Jhung, J.H. Lee, J.W. Yoon, C. Serre, G. Férey, J.S. Chang
Adv. Mater., 19 (2007), pp. 121-124
CrossRef View Record in Scopus

[34] G. Sargazi, D. Afzali, A. Mostafavi
Ultrason. Sonochem., 41 (2018), pp. 234-251
Article Download PDF View Record in Scopus

[35] G. Sargazi, D. Afzali, A. Mostafavi
Appl. Organomet. Chem., 33 (2019), p. e4816
CrossRef View Record in Scopus

[36] S. Gaikwad, S. Han
Chem. Eng. J., 371 (2019), pp. 813-820
Article Download PDF View Record in Scopus

[37] S. Han, Y. Huang, T. Watanabe, S. Nair, K.S. Walton, D.S. Sholl, J.C. Meredith
Microporous Mesoporous Mater., 173 (2013), pp. 86-91
Article Download PDF View Record in Scopus

[38] S.R. Caskey, A.G. Wong-Foy, A.J. Matzger
J. Am. Chem. Soc., 130 (2008), pp. 10870-10871
CrossRef View Record in Scopus

[39] P. Mishra, S. Edubilli, B. Mandal, S. Gumma
Microporous Mesoporous Mater., 169 (2013), pp. 75-80
Article Download PDF View Record in Scopus

[40] Z. Zhang, S. Xian, H. Xi, H. Wang, Z. Li
Chem. Eng. Sci., 66 (2011), pp. 4878-4888
Article Download PDF View Record in Scopus

[41] K. Munusamy, G. Sethia, D.V. Patil, P.B.S. Rallapalli, R.S. Somani, H.C. Bajaj
Chem. Eng. J., 195 (2012), pp. 359-368
Article Download PDF View Record in Scopus

[42] D. Saha, Z. Bao, F. Jia, S. Deng
Environ. Sci. Technol., 44 (2010), pp. 1820-1826
CrossRef View Record in Scopus

[43] S. Gaikwad, S.-J. Kim, S. Han
Microporous Mesoporous Mater., 277 (2019), pp. 253-260
Article Download PDF View Record in Scopus

[44] C. Choi, R.L. Kadam, S. Gailwad, K.-S. Hwang, S. Han
Microporous Mesoporous Mater. (2020), p. 110006
Article Download PDF View Record in Scopus

[45] H.Y. Huang, R.T. Yang, D. Chinn, C.L. Munson
Ind. Eng. Chem. Res., 42 (2003), pp. 2427-2433
CrossRef View Record in Scopus

[46] Y. Chen, D. Lv, J. Wu, J. Xiao, H. Xi, Q. Xia, Z. Li
Chem. Eng. J., 308 (2017), pp. 1065-1072
Article Download PDF View Record in Scopus

[47] D. Qian, C. Lei, G.-P. Hao, W.-C. Li, A.-H. Lu
ACS Appl. Mater. Interfaces, 4 (2012), pp. 6125-6132
CrossRef View Record in Scopus

[48] F. Gao, Y. Li, Z. Bian, J. Hu, H. Liu
J. Mater. Chem., 3 (2015), pp. 8091-8097
CrossRef View Record in Scopus

[49] S. Xian, F. Xu, C. Ma, Y. Wu, Q. Xia, H. Wang, Z. Li
Chem. Eng. J., 280 (2015), pp. 363-369
Article Download PDF View Record in Scopus

[50] R. Banerjee, H. Furukawa, D. Britt, C. Knobler, M. O'Keeffe, O.M. Yaghi
J. Am. Chem. Soc., 131 (2009), pp. 3875-3877
CrossRef View Record in Scopus

[51] A.O.z.r. Yazaydın, R.Q. Snurr, T.-H. Park, K. Koh, J. Liu, M.D. LeVan, A.I. Benin, P. Jakubczak, M. Lanuza, D

J. Am. Chem. Soc., 131 (2009), pp. 18198-18199
CrossRef View Record in Scopus

[52] J. Liu, J. Tian, P.K. Thallapally, B.P. McGrail
J. Phys. Chem. C, 116 (2012), pp. 9575-9581
CrossRef View Record in Scopus

[53] D.M. Ruthven
Principles of Adsorption and Adsorption Processes
John Wiley & Sons, New York (1984)
Google Scholar

[54] J. Schindelin, I. Arganda-Carreras, E. Frise, V. Kaynig, M. Longair, T. Pietzsch, S. Preibisch, C. Rueden, S. Saalfeld, B. Schmid
Nat. Methods, 9 (2012), p. 676
CrossRef View Record in Scopus

[55] S. Han, Y. Huang, T. Watanabe, Y. Dai, K.S. Walton, S. Nair, D.S. Sholl, J.C. Meredith
ACS Comb. Sci., 14 (2012), pp. 263-267
CrossRef View Record in Scopus

[56] Q. Yang, C. Xue, C. Zhong, J.F. Chen
AIChE J, 53 (2007), pp. 2832-2840
CrossRef View Record in Scopus

[57] R.V. Siriwardane, M.-S. Shen, E.P. Fisher, J.A. Poston
Energy Fuels, 15 (2001), pp. 279-284
View Record in Scopus

[58] H.-Y. Chen, M. Kollar, Z. Wei, F. Gao, Y. Wang, J. Szanyi, C.H. Peden
Catal. Today, 320 (2019), pp. 61-71
Article Download PDF CrossRef View Record in Scopus

[59] Q. Xie, F. Li, H. Guo, L. Wang, Y. Chen, G. Yue, D.-L. Peng
ACS Appl. Mater. Interfaces, 5 (2013), pp. 5508-5517
CrossRef View Record in Scopus

[60] C. Zhu, Z. Zhang, B. Wang, Y. Chen, H. Wang, X. Chen, H. Zhang, N. Sun, W. Wei, Y. Sun
Microporous Mesoporous Mater., 226 (2016), pp. 476-481
Article Download PDF View Record in Scopus

[61] D.J. Tranchemontagne, J.R. Hunt, O.M. Yaghi
Tetrahedron, 64 (2008), pp. 8553-8557
Article Download PDF View Record in Scopus

[62] S. Salehi, M. Anbia
Energy Fuels, 31 (2017), pp. 5376-5384
CrossRef View Record in Scopus

[63] Z. Zhao, Z. Li, Y. Lin
Ind. Eng. Chem. Res., 48 (2009), pp. 10015-10020
CrossRef View Record in Scopus

[64] T. Zhao, F. Jeremias, I. Boldog, B. Nguyen, S.K. Henninger, C. Janiak
Dalton Trans., 44 (2015), pp. 16791-16801
CrossRef View Record in Scopus

[65] Q. Liu, L. Ning, S. Zheng, M. Tao, Y. Shi, Y. He
Sci. Rep., 3 (2013), p. 2916
View Record in Scopus

[66] Z. Zhou, L. Mei, C. Ma, F. Xu, J. Xiao, Q. Xia, Z. Li
Chem. Eng. Sci., 147 (2016), pp. 109-117
Article Download PDF View Record in Scopus

[67] M. Taddei, P.V. Dau, S.M. Cohen, M. Ranocchiari, J.A. van Bokhoven, F. Costantino, S. Sabatini, R. Vivani
Dalton Trans., 44 (2015), pp. 14019-14026
CrossRef View Record in Scopus

[68] H.T. Nguyen, Y. Tran, H.N. Nguyen, T.C. Nguyen, F. Gándara, P.T. Nguyen
Inorg. Chem., 57 (2018), pp. 13772-13782
CrossRef View Record in Scopus

View Abstract